Nanoscale

PAPER

View Article Online
View Journal | View Issue

Cite this: *Nanoscale*, 2022, **14**, 9474

Copper metal organic framework as natural oxidase mimic for effective killing of Gram-negative and Gram-positive bacteria†

Zhihui Mao,‡[a,b] Jie Chen,‡[b,c] Yindian Wang,[b] Junjie Xia,[b] Yajing Zhang,[d] Weiwen Zhang,[d] Han Zhu,[b] Xiaojun Hu*[b] and Hongxia Chen *[b]

Received 26th March 2022,
Accepted 2nd June 2022

DOI: 10.1039/d2nr01673g

rsc.li/nanoscale

Nanozymes have been widely studied as substitutes for natural enzymes. However, the delicacy of their structures and their unclear catalytic sites make it difficult to maintain their structural robustness and catalytic durability. By mimicking active catalytic sites of natural enzymes and combining them with distinct channels of metal organic frameworks (MOFs), an active copper mimetic oxidase enzyme (Cu-MOF) was designed and synthesized with good structure and clear catalytic sites for improvement in catalytic activity. The Cu-MOFs showed excellent oxidase-like activity with a low K_m of 1.09 mM and exogenous ROS generation capacity. The Cu-MOFs exhibited antibacterial efficacy at a low concentration of 12.5 μg mL^{-1} by an oxidative stress response. These Cu-MOFs with their simple design and effective oxidase mimicking show attractive application prospects in the field of antibacterial and enzyme catalysis.

1 Introduction

Nanozymes have gradually become the preferred substitutes for natural enzymes due to their low cost, stress resistance, high-throughput preparation and ability to overcome the limitations of natural enzymes.[1–3] Until now, many nanozymes have been reported, such as metal oxides mimicking peroxidase,[4,5] and metal–organic frameworks (MOFs) mimicking peroxidase.[6] Benefitting from applications of nanozymes, significant advances have been achieved in catalysis science, biosensors, therapeutic applications, environmental protection and antibacterial agents.[7] Although impressive progress has been made so far, it is still a challenge to fully realize the potential of nanozymes in this field.[8] Most artificial enzymes, such as Fe_3O_4, have been based on peroxidase-like activity and unstable H_2O_2 as a sacrificial oxidant.[9,10] The effect of localized field enhancement on electron transfer induced by surface plasmon resonance (SPR) of noble metal nanoparticles and its composites makes them an excellent candidate for nanozymes.[11,12] However, the previously reported metal oxides and noble metal nanomaterials still show peroxidase-like activity in simulated oxidases,[13,14] and their inferior enzyme activity and high preparation cost restrict the practical application of these materials. However, the widespread presence of H_2O_2 is severely restrictive, and the extra addition of easily decomposable, volatile and highly toxic H_2O_2 severely restricts the promotion of nanoenzymes. Compared with H_2O_2, O_2 naturally dissolved in solution is highly stable and mild, so oxidase nanozymes have attracted extensive attention due to their oxidation mechanism by directly activating O_2 to yield reactive oxygen species (ROS), avoiding the participation of H_2O_2,[15,16] and making them green catalysts.[17]

In recent years, some nanozymes have been reported to imitate the structure of natural enzymes, which provide a possible solution for the design and synthesis of new artificial oxidases.[18,19] In an oxygen-activating natural oxidase, a transition metal plays a wide variety of roles of a natural enzyme on the basis of its generally accessible redox couple and bioavailability,[20] such as in hemocyanin,[21] tyrosinases,[22] dopamine β-monooxygenase (DβM)[23] and catechol oxidase (CatO).[24] Among many proteases, reactive copper is an important kind of catalytically active center, which can catalyze dehydrogenation.[25,26] The electron transfer of an active copper center overcomes the spin-forbidden-ness of O_2 binding and controls electron transfer to direct catalysis, performing either two-electron electrophilic aromatic substitution or one-electron H-atom abstraction.[27,28] Therefore, by imitating a copper catalytic site, it provides a feasible idea for the rational design

[a]School of Environmental and Chemical Engineering, Shanghai University, Shanghai 200444, China
[b]School of Life Sciences, Shanghai University, Shanghai, 200444, China. E-mail: hxchen@shu.edu.cn, xjhu11@shu.edu.cn
[c]School of Medicine, Shanghai University, Shanghai, 200444, China
[d]School of Qianweichang, Shanghai University, Shanghai, 200444, China

†Electronic supplementary information (ESI) available. See DOI: https://doi.org/10.1039/d2nr01673g

‡These authors contributed equally to this work

of new and improved biomimetic catalysts.[29,30] However, the macroscopically rough preparation process of artificial oxidases leads to the loss of nanoscale fine structure, which makes it difficult to imitate the natural enzyme's inherent catalytic structure such as catalytically activity centers as well as substrate binding sites.[31,32] Finding an artificial oxidase with a fine secondary structure and cost advantages is urgent.[33]

MOFs, a kind of multifunctional porous coordination polymer,[34] are composed of organic bridging molecules (ligands) and metal ions or metal clusters.[35–37] The internal structure and surface physicochemical properties of MOFs can be controlled by the selection of metal ion centers or organic ligands.[38,39] In addition, the size and shape of a MOF crystal can be reasonably adjusted by the selection of temperature, solvent and reaction time in the synthesis process.[40,41] The diversity of metallic nodes, bridging ligands, and a wide array of coordination interactions in all possible directions make MOFs direct surrogates for artificial oxidases,[42] where the well-defined tailorable cavities and channels can offer a hydrophobic coordination environment similar to that of natural enzymes.[43] Until now, there have been few submissions about MOFs applied to artificial oxidases.[44] Through the pre-structural design and regulation of the preparation process, the catalytic activity and substrate selectivity of a nanozyme can be reasonably adjusted; therefore, MOF-based artificial nanomaterials are expected to improve the performance of nanozymes.

Herein, we have designed and synthesized an active copper artificial oxidase based on Cu-MOFs which can catalyze the oxidation of 3,3′,5,5′-tetramethylbenzidine (TMB) with the absence of additional H_2O_2. 3-Amino-5-mercapto-1,2,4-triazole (AMTA)[45] not only has potential biological activity (treating viral as well as bacterial infection) due to nitrogen and sulfur heterocyclic systems but also has potential as a multifunctional ligand in coordination chemistry which can bind strongly to Cu^{2+} ions *via* N–Cu coordination to afford a catalytic center. As a result, AMTA was selected as a ligand in this catalytic system. By incorporation of the triazole unit in the structure of Cu-MOFs, the generation efficiency of reactive oxygen species (ROS) was effectively improved.[46] Cu-MOFs show excellent oxidase-like activity at a very low concentration; furthermore, the oxidase-like activity and exogenous ROS generation were used in research against *E. coli* and *S. aureus* bacterial strains. The antibacterial results showed that Cu-MOFs have stronger antibacterial activity. To the best of our knowledge, this is the first time that Cu-MOFs alone have shown good oxidase activity in the absence of a second noble metal component (Scheme 1).

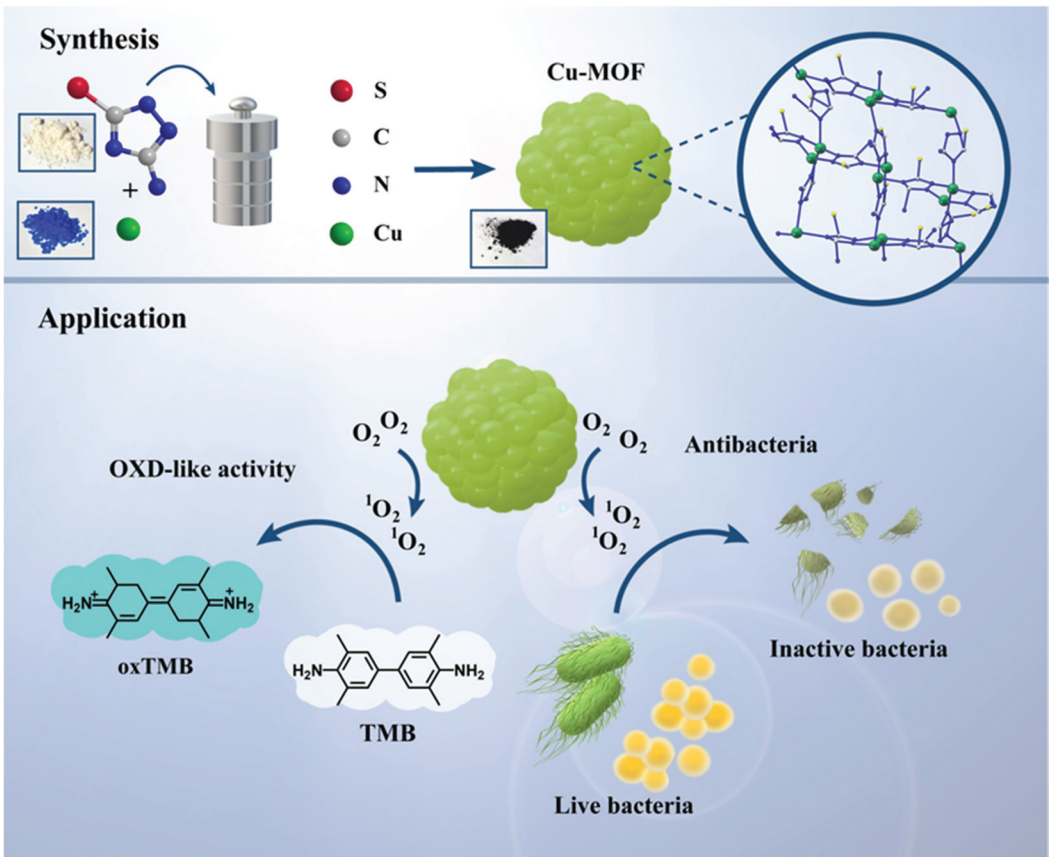

Scheme 1 Schematic illustration of the synthesis and oxidase-like activity of Cu-MOFs with their antibacterial presentation.

2 Experimental section

2.1 Reagents

Copper(II) nitrate hydrate ($Cu(NO_3)_2{\cdot}2.5H_2O$) was obtained from Sigma-Aldrich Co., Ltd. AMTA and *N*,*N*-dimethylformamide (DMF) were purchased from Shanghai Aladdin Biochemical Technology Co., Ltd. Anhydrous ethanol (C_2H_5OH), sodium borohydride ($NaBH_4$, 96.0%) were of analytical grade (AR) and purchased from China Medicine (Group) Shanghai Chemical Reagent Corp. All chemical reagents were used as received without further purification. Deionized water (18.4 MΩ cm) was used for all experiments and was obtained from a Milli-Q system (Millipore, Bedford, MA).

2.2 Instruments

The morphology and size of the sample were visualized using a scanning electron microscope (SEM; Nova Nano SEM 450, American). The crystallinity and the purity of the particles were determined by X-ray diffraction (XRD; D8A25, Bruker, Germany) using Cu Kα radiation (λ = 1.54051 and 1.54433 Å) over the 2θ range of 3°–80°. Transmission electron microscope (TEM) images were taken with a JEOL JEM 2100F at an accelerating voltage of 200 kV. The JEOL JEM 2100F is also equipped with an energy dispersive X-ray spectrometer (EDX) system, allowing the elemental analysis of the samples. The copper ions were measured by atomic absorption spectroscopy (AA-6300 double-beam flame spectrophotometer; Shimadzu, Europe) and inductively coupled plasma mass spectrometry (ICP-MS; Thermo Fisher, Shanghai). Fourier transform infrared (FT-IR) spectra were collected on a JASCO FT-IR 480 Plus spectrophotometer. UV-visible spectra were recorded on a Shimadzu UV2501 spectrophotometer. Zeta potential (Zeta; Malvern, UK) was measured to detect the positive and negative charges of the sample solution. Dynamic light scattering (DLS; Malvern, UK) was utilized to detect the particle size distribution. Cyclic voltammetry (CV) was performed with an electrochemical workstation (CHI660C) and a typical three-electrode system.

2.3 Preparation of the Cu-MOFs

$Cu(NO_3)_2{\cdot}2.5H_2O$ (697.8 mg, 3 mmol) and AMTA (522.6 mg, 4.5 mmol) were placed in 100 mL of a DMF/C_2H_5OH solvent mixture (DMF : C_2H_5OH = 1 : 1) and heated for 12 h at 120 °C. After centrifugation, the sediment was rinsed repeatedly with C_2H_5OH and DMF and heated for 24 h at 120 °C in a vacuum. The obtained product was named Cu-MOFs.

2.4 Oxidase-like activity of Cu-MOFs

The oxidase-like activity of Cu-MOFs was evaluated by using TMB as a substrate molecule for a colorimetric assay. Typically, 2.5 mM TMB and 0.1 mg mL^{-1} Cu-MOFs were mixed with acetate buffer solution (pH = 4), followed by incubation at 40 °C with constant oscillation for 10 min in a thermostatic mixed-metal bath. Finally, the absorbance of oxidized TMB at 652 nm was measured using a UV-vis spectrophotometer. As a control group, the oxidase activities of ($Cu(NO_3)_2{\cdot}2.5H_2O$) and AMTA were investigated using the same experimental procedure.

ABTS was also used to investigate the enzyme-like activity of Cu-MOFs. 2.5 mM ABTS was added to 0.1 mg mL^{-1} Cu-MOFs with acetate buffer solution (pH = 4), followed by incubation at 40 °C with constant oscillation for 10 min in a thermostatic mixed-metal bath. The absorbance of oxidized ABTS at 430 nm was recorded on a UV-vis spectrophotometer.

2.5 Kinetic and mechanism analysis

The kinetics of TMB catalysis was monitored in a time-scan mode with the absorption spectra at 652 nm. Cu-MOFs (0.5 mg) and different concentrations of TMB (0.05, 0.1, 0.25, 0.5, 0.75, 1.0 mM) were mixed with acetate buffer solution (pH = 4). After that, the reaction was monitored immediately. The relevant kinetic parameters were calculated according to the Michaelis–Menten equation:

$$\nu = \frac{\nu_{max} \times [S]}{K_m + [S]} \quad (1)$$

where ν is the initial velocity, ν_{max} is the maximal reaction velocity, K_m is the Michaelis constant, and [S] is the substrate concentration.

To explore the mode of action for Cu-MOFs oxidase-like enzyme activity, active species-scavenging experiments were conducted. A scavenger of singlet oxygen ($^1O_2$) or hydroxyl radical ($^{\bullet}OH$) was added to a mixed solution of Cu-MOFs and TMB, followed by incubation for 10 min. Finally, the absorbance spectrum of oxidized TMB was recorded.

2.6 Verification of antibacterial ability

To examine the antibacterial ability of Cu-MOFs against Gram bacteria, two strains were used as representatives of different types of Gram bacteria. *E. coli* was used as an example of Gram-negative bacteria, and *S. aureus* was used as the representative of Gram-positive bacteria. All the bacterial strains were stored at 4 °C and reactivated by incubating the bacteria in 100 mL of medium at 37 °C with 150 rpm shaking overnight until the density of the bacteria reached 10^8 colony forming units (CFU) per mL.

To assess the sterilization ability of Cu-MOFs, comparative experiments were conducted. By setting the concentration of Cu-MOFs at 0, 0.25, 0.5, 12.5, 25, and 50 μg mL^{-1}, bacterial solutions and antibacterial material solutions were mixed at a volume ratio of 1 : 1, followed by spreading of the mixture on an agar plate and incubating overnight. The antibacterial ability of Cu^{2+} and AMTA was investigated by the same experimental procedure. The structural stability of Cu-MOFs before and after co-culture with bacteria was determined by measuring the content of Cu^{2+} in the supernatant.

2.7 Live/dead fluorescence assay

Gram-negative bacteria (*E. coli*) and Gram-positive bacteria (*S. aureus*) suspensions were centrifuged at 2000 rpm and washed with PBS three times, and finally resuspended in PBS. Cu-

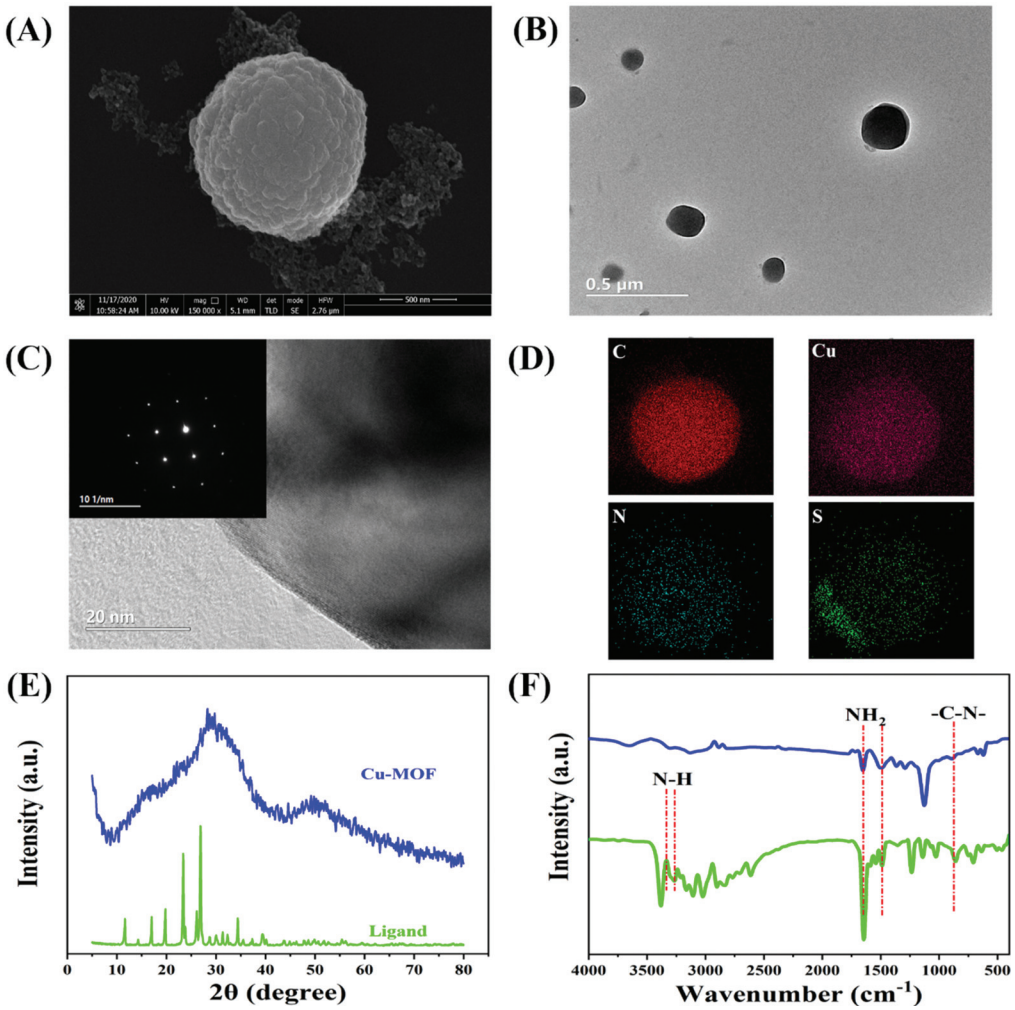

Fig. 1 SEM images of uniform Cu-MOF nanoparticles (A). TEM image of Cu-MOF nanoparticles at low magnification (B). TEM image extracted from a part of a Cu-MOF nanoparticle; inset is the corresponding FFT pattern of Cu-MOF nanoparticles (C). EDS mapping of Cu-MOF nanoparticles (D). XRD and FTIR spectral analysis of bridging ligand, Cu-MOFs (E) and (F).

MOFs (0.5 μg) were added into 1 mL of *E. coli* and *S. aureus* suspensions, respectively, and then incubated at 37 °C for 12 h. After that, the suspensions were pelleted at 2000 rpm to obtain bacteria and resuspended in PBS. SYTO-9 and propidium iodide (PI) were added to the treated bacteria and stained in the dark with for 0.5 h. Fluorescence images were achieved by using a fluorescence inverted microscope.

3 Results and discussion

3.1 Characterization of Cu-MOFs

The morphology of the prepared Cu-MOFs was characterized by SEM. Fig. 1(A) shows that the Cu-MOFs have a good spherical structure. TEM images were collected to characterize the obtained Cu-MOFs, as revealed in Fig. 1(B), where the overall nanoparticle size is estimated to about 300 nm, and the clear edge frame structure of Cu-MOFs shows that the nanoparticles have become compact, which is conducive to an improvement in the stability of the Cu-MOFs. The fast Fourier transform (FFT) pattern of the Cu-MOFs is shown in the inset to Fig. 1(C) with a lattice spacing of ~0.206 nm (Fig. S1†), which is evidence of the crystal structure of the Cu-MOFs. It can be inferred that the formation of a good spherical structure is based on the process of crystallization and the Ostwald ripening process.[47] First, Cu^{2+} unite with the AMTA ligands to form amorphous solid spherical particles. After a further solvothermal reaction, the amorphous solid spherical particles tend to crystallize under conditions of continuous high pressure and high heat, and self-assembly to gradually form larger spherical crystals.[48] Elemental mapping by EDX (Fig. 1(D)) revealed that the Cu-MOFs consist of homogeneously distributed Cu, C, N, S elements. The crystal structure of the Cu-MOFs was further characterized by XRD. After coordination between AMTA and Cu^{2+}, the characteristic peaks belonging to AMTA disappear. Due to the incomplete crystallization effect, the pure Cu-MOFs did not show sharp and obvious diffraction peaks, and exhibited characteristic diffraction peaks (2θ = 30°)

in agreement with previous reports.[49] The FTIR spectra of AMTA and Cu-MOFs are shown in Fig. 1(F). For pure AMTA, the band at 3381 cm^{-1} is assigned to ν(N–H) of the ligand, and disappeared in Cu-MOFs; this observation demonstrates that the amino group coordinated with Cu. The inconspicuous new peaks of Cu-MOFs at 3323 cm^{-1} also proved the effect of the coordination process on AMTA. A band occurs at 1655 cm^{-1} assigned to NH_2 bending vibration. As the nitrogen atom on the imidazole ring is coordinated with a copper ion, similar atoms outside the ring can be retained in Cu-MOFs. Similarly, the triazole ring stretching band occurring at 1496 cm^{-1} is also retained. The C–N stretching vibration could be evidenced by the band at 1134 cm^{-1}.

The thermal stability of the structure for the prepared Cu-MOFs was explored by thermogravimetric analysis. The individual ligands have an obvious thermally stable platform (0–280 °C). Above 280 °C, the ligands will sublime. The quality of the prepared Cu-MOFs is reduced due to the volatilization of crystal water at 0–150 °C. Above 150 °C, the weight loss can be attributed to degradation of the framework structure, and this leads to the oxidation of some Cu. Although the quality of Cu-MOFs is slowly reduced, they still have a mass retention rate of more than 70% at 400 °C, indicating their relatively excellent thermal stability (Fig. 2(A)). Due to the mild application environment (nanozyme catalysis, antibacterial), the thermal stability of Cu-MOFs guarantees their excellent stability in the operating temperature range. As a typical porous material, the porous structure brings about a larger accessible surface, which is conducive to the adsorption of dissolved oxygen and the generation of ROS, and the pores of Cu-MOFs provide active sites similar to those of natural enzymes, which help increase enzyme activity. As shown in Fig. 2(B), the N_2 adsorption–desorption isotherm of Cu-MOFs belongs to the type IV isotherm, corresponding to typical mesoporous materials. The BET surface area was calculated as 212.793 $m^2\ g^{-1}$, and the pore size distributions for Cu-MOFs are shown in the inset to Fig. 2(B).

The surface chemical composition and oxidation state of an enzyme have a significant effect on the catalytic ability of the enzyme. CV curves of bare electrodes and Cu-MOF-modified electrodes are compared in Fig. 3(A). There are two characteristic peaks at 0.11 and 0.38 V in 0.5 M H_2SO_4 under 50 mV s^{-1} conditions, corresponding to the reduction peaks of Cu^{2+}. The presence of Cu in the composites as well as the oxidation state were confirmed using high-resolution X-ray photoelectron spectroscopy (XPS). Fig. 3(B) reveals the spectra of Cu-MOFs. The peaks of Cu 2p, N 1s, and S 2p appeared in the spectra. Fig. 3(C) shows the core-level and shakeup satellite (sat.) lines of Cu 2p.[50] The Cu 2p3/2 and 2p1/2 core levels are located at binding energies of 932.7 and 955.2 eV, and are close to the data for Cu^{2+}, which shows the divalent nature of the Cu atoms, which are thus expected to be effective active sites during catalysis. Several strong satellite peaks (at 963.4, 943.4 eV) were easy to observe. Fig. 3(D) shows two peaks of N 1s at 400.5 and 402.1 eV. Pyrrole nitrogen (N–H) at 402.1 eV was significantly lower than C=N at 400.5 eV, confirming the formation of Cu-MOFs.

3.2 Oxidase-like activity of Cu-MOFs

TMB and ABTS, as well-established chromogenic substrate molecules, were utilized to investigate the oxidase-like activity of Cu-MOFs without the help of additional H_2O_2.[51] In the model reaction of catalytic oxidation of TMB (Fig. 4(A)) and ABTS (Fig. 4(B)), they are able to show a clear color change from colorless to blue or green. Fig. 4(C) presents the results of the oxidase activity analysis of Cu-MOFs. ROS generated by Cu-MOFs can catalyze TMB to oxidase TMB (blue color) with maximal absorbance at 652 nm, but the TMB or Cu-MOFs only groups show no color change or absorption at 652 nm. Similarly, oxidized ABTS shows a green color under the catalysis of Cu-MOFs and has a maximal absorbance at 430 nm in Fig. 4(D). For comparison, the single Cu-MOFs or ABTS groups show no color change and the absorbance at 430 nm is unprecedented. $Cu(NO_3)_2{\cdot}2.5H_2O$ and AMTA alone do not show any enzymatic activity (Fig. S4†). These results clearly verify the strong oxidase-like activity of Cu-MOFs.

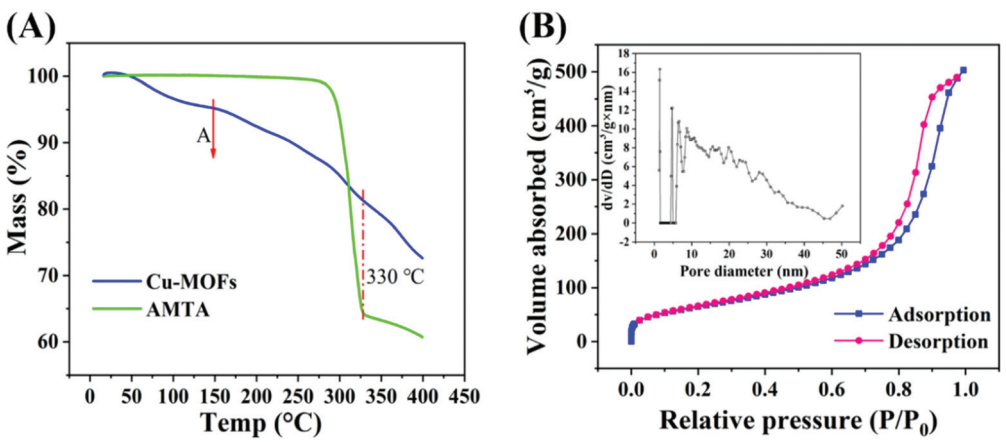

Fig. 2 (A) TGA curve of Cu-MOFs (blue), AMTA (green). (B) N_2 adsorption–desorption isotherm; inset is the pore size distribution.

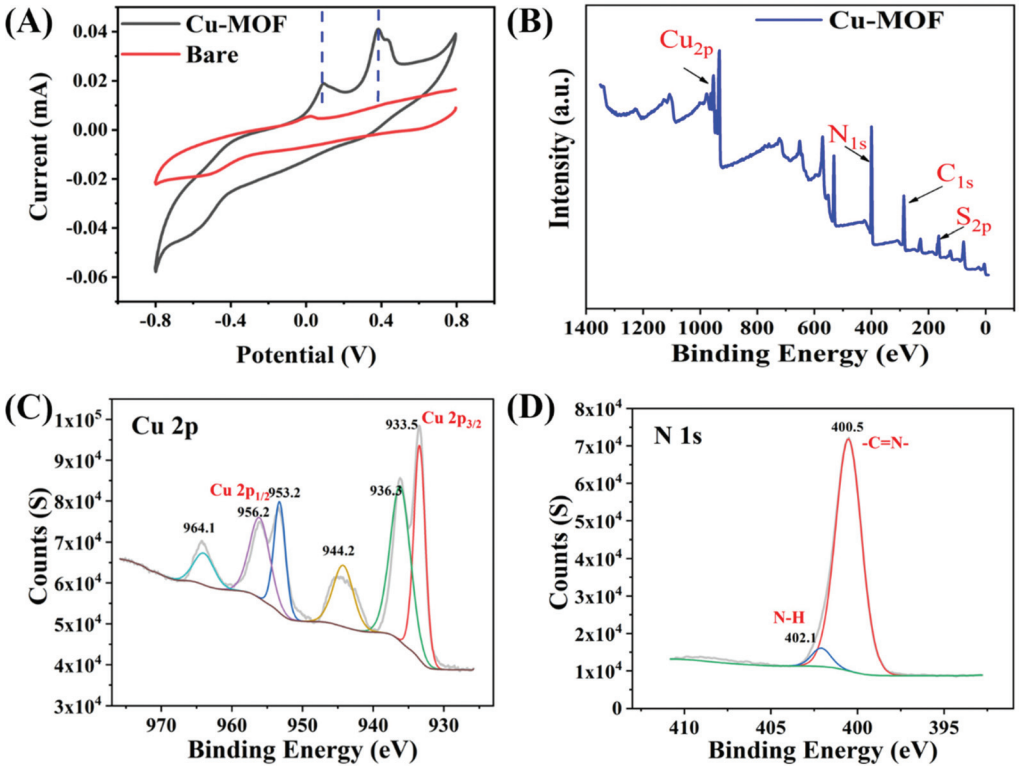

Fig. 3 CV curves of the Cu-MOFs in 0.5 M H_2SO_4 at 50 mV s^{-1} (A). XPS survey scan of Cu-MOFs (B). Cu 2p (C) and N 1s (D) XPS spectrum of Cu-MOFs.

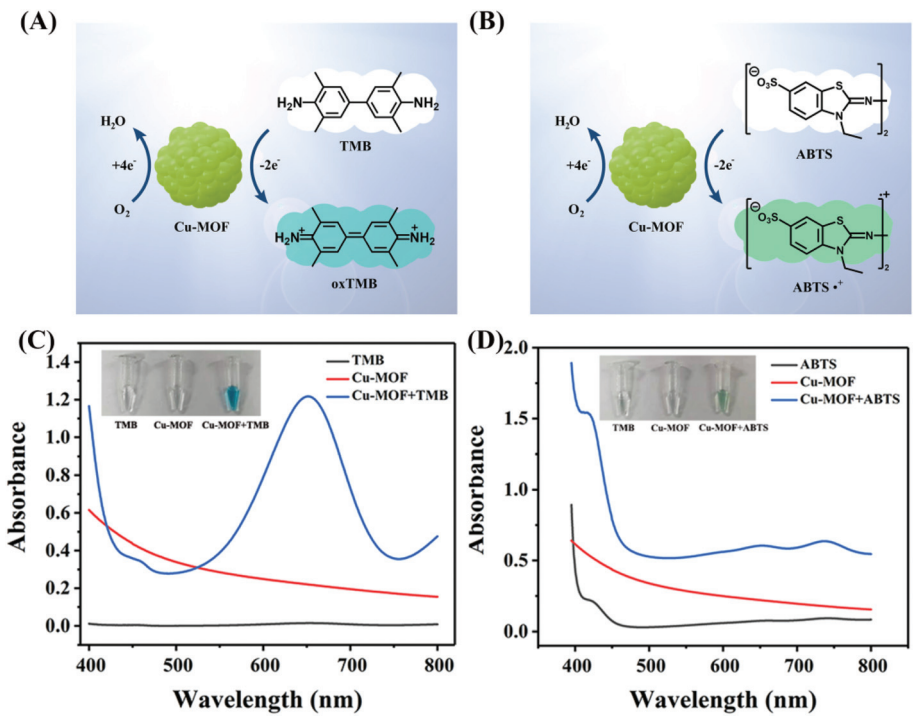

Fig. 4 Schematic illustration of the oxidase-like activity of Cu-MOFs for TMB (A) and ABTS (B). The UV-vis spectra of TMB (C) and ABTS (D) in the absence and presence of Cu-MOFs. Inserts: the color change of the corresponding solution.

The catalytic activity of a natural enzyme is affected by its reaction conditions. Fig. S2† shows the effect of reaction conditions on the oxidase-like activity of prepared Cu-MOFs, like the pH, temperature, and concentration of Cu-MOFs. Fig. S2 (A)† shows the absorption at 652 nm of the Cu-MOFs + TMB reaction systems under different pH from 3 to 8 and the optimum pH was found to be 4.0. The Cu-MOFs presented better catalytic activity over a wide temperature range (4–60 °C), which is shown in Fig. S2(B).† The catalytic effect was enhanced with increasing Cu-MOFs concentration (Fig. S2 (C)).† When the concentration of Cu-MOFs was 0.5 mg mL^{-1}, the absorbance reached its optimum. Therefore, the optimum catalytic pH and Cu-MOFs concentration are nearly 4 and 0.5 mg mL^{-1}, respectively. To investigate the stability over time of Cu-MOFs in aqueous medium, the Cu-MOF dispersion was stored at room temperature and the oxidase activity was tested for 4 weeks continuously. As shown in Fig. S3,† there were no remarkable changes in the oxidized TMB intensity after 28 days, indicating the satisfactory long-term stability of the Cu-MOFs.

3.3 Kinetic and mechanism analysis

To verify the catalytic mechanism, a kinetic study was conducted by steady-state kinetics experiments. According to time-dependent absorbance at 652 nm with different concentrations of TMB in the presence of 0.5 mg mL^{-1} (Fig. 5(A)), the kinetics plot was obtained and is shown in Fig. 5(B), which followed Michaelis–Menten kinetics.[52] V_{max} and K_m were calculated from the kinetics plot as 17.06 μM s^{-1} and 1.09 mM, respectively. The V_{max} value represents the catalytic activity of Cu-MOFs, and the high value indicates stronger catalytic activity. Compared with other nanozymes listed in Table S1,† Cu-MOFs exhibited a higher catalytic activity and affinity, which may be associated with the copper metal center and larger specific surface area of Cu-MOFs.[53]

As oxidase nanozymes, Cu-MOFs were assumed to have an oxidase-type mechanism by activating O_2 to yield ROS. Fig. 5 (C) shows the effect of O_2 on oxidase-like activity. Compared to the absorbance of control groups, the absorbance of TMB catalyzed by Cu-MOFs was significantly inhibited in N_2-saturated buffer, indicating that O_2 plays an important role in this reaction. To understand the catalysis mechanism of Cu-MOFs between oxidase and peroxidase-like activity, a fluorescent assay with terephthalic acid (TA) was conducted to investigate the possibility of peroxidase-like activity. It is well known that peroxidase-like nanozymes can catalyze H_2O_2 to generate $^{\bullet}OH$ which converts non-fluorescent TA to highly fluorescent 2-hydroxy terephthalic acid (TAOH). In Fig. 5(D), the TA itself and Cu-MOFs/H_2O_2 have no fluorescence peak at 435 nm, while a distinct fluorescence peak can be observed in H_2O_2/TA due to the self-decomposition of H_2O_2. After the addition of Cu-MOFs, there is no clear enhancement in the emission peak, and this strongly indicates that Cu-MOFs did not depend on peroxidase-like activity at the same time.

To figure out the model of action for the oxidase-like activity of Cu-MOFs, an ROS-scavenging experiment was performed. L-Histidine and isopropanol were added into Cu-MOFs + TMB reaction systems, as quenchers of single oxygen ($^1O_2$) and hydroxyl radicals ($^{\bullet}OH$), respectively. As shown in Fig. 5(E and F), L-histidine effectively suppressed the oxidation

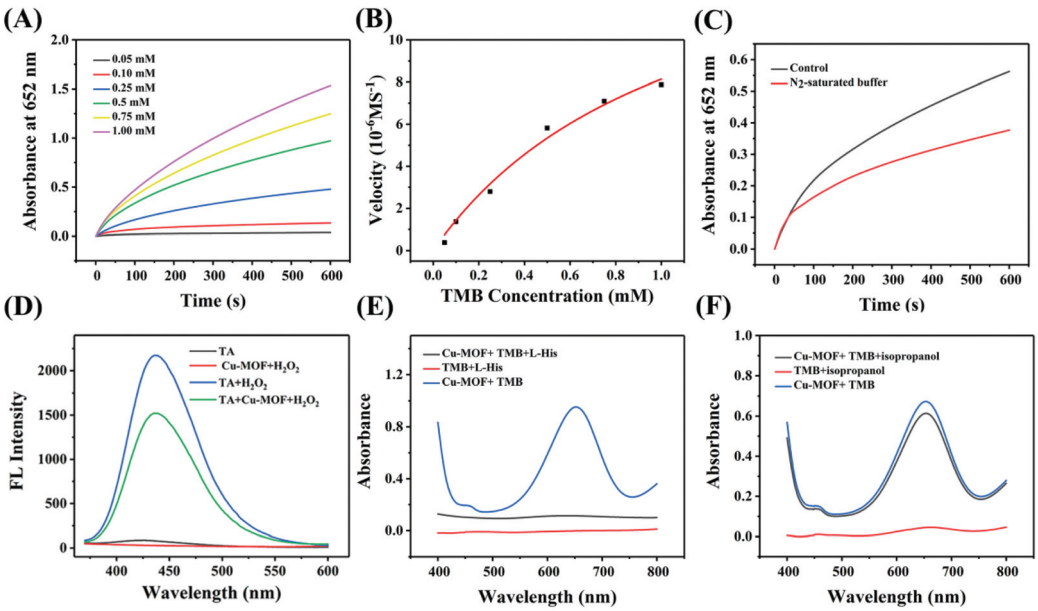

Fig. 5 Time-dependent absorbance at 652 nm with different concentrations of TMB in the presence of 0.5 mg mL^{-1} Cu-MOFs (A). Michaelis–Menten kinetic assay for TMB (B). UV-vis absorption spectra of TMB in air-saturated and N_2-saturated buffer with Cu-MOFs (C). The fluorescence spectra of the TA assay for the detection of hydroxyl radicals ($^{\bullet}OH$) (D). Absorbance at 652 nm of TMB to estimate the nature of the intermediates for the oxidase-like activity of Cu-MOFs (0.5 mg mL^{-1}) in the presence of various quenchers (E and F).

of TMB, but the absorbance of the group with isopropanol showed no significant difference from the control, indicating that the formation of $^1O_2$ is the prominent reason for the oxidase-like activity of Cu-MOF instead of $^{\bullet}OH$. The result further verified the oxidation mechanism of Cu-MOFs by activating O_2 to produce $^1O_2$.

3.4 Antibacterial performance of Cu-MOFs

ROS is able to destroy the bacterial membrane to inhibit bacterial growth through oxidative stress. Based on their outstanding oxidase-like activity, Cu-MOFs can induce O_2 to produce $^1O_2$; therefore the antibacterial ability was studied. An antibacterial experiment was conducted to evaluate the antibacterial efficacy of Cu-MOFs against *E. coli* and *S. aureus*. Fig. 6(A) shows the relationship between antibacterial performance against *E. coli* and *S. aureus* with the concentration of Cu-MOFs from 0 to 50 μg mL^{-1}. With the increasing concentration of Cu-MOFs, the antibacterial rate increased from 0% to 100%, which indicated that Cu-MOFs with higher concentration had better antibacterial properties. When the concentration of Cu-MOFs reached 25 μg mL^{-1}, the antibacterial ratio could reach 99.9%. Compared with *E. coli*, the antibacterial efficacy against *S. aureus* of Cu-MOFs is more obvious, owing to *E. coli* having a multilayer outer membrane and strong drug resistance. The above results indicated that Cu-MOFs displayed good broad-spectrum antibacterial ability at low concentration. 12.5 μg mL^{-1} of Cu-MOFs was selected to verify the time-dependent antibacterial properties against *E. coli* and *S. aureus* in the time range of 0 to 40 minutes; the results are shown in Fig. S5.† The antibacterial rate increased with increasing incubation time with Cu-MOFs. When the incubation time reached 40 min, the antibacterial ratio could reach 99.9%, which confirms that Cu-MOFs have satisfactory antibacterial ability against *E. coli* and *S. aureus* within 40 min.

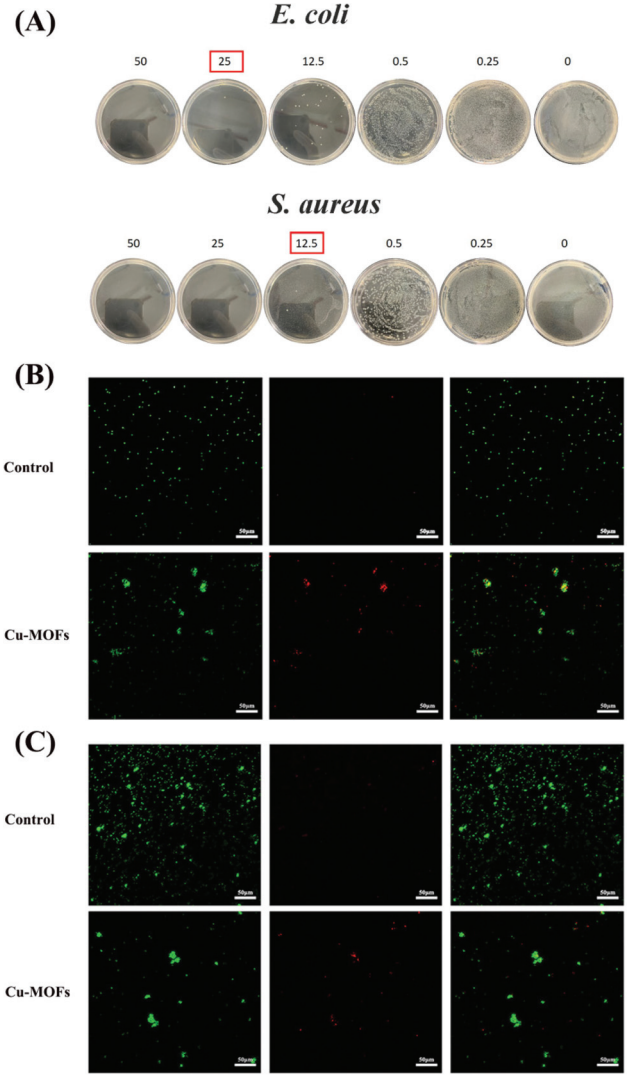

Fig. 6 Antibacterial performance against *E. coli* and *S. aureus* (A) of Cu-MOFs with concentrations from 0 to 50 μg mL^{-1}. (B and C) Fluorescence images of *E. coli* (B) and *S. aureus* (C) that had undergone Cu-MOFs treatment. Live bacteria (green) and dead bacteria (red).

To further assess the effect of the Cu-MOFs on bacterial cell viability and morphology, a live/dead staining experiment was conducted and is revealed in Fig. 6(B) and (C). SYTO-9 (green channel), as a cell-permeant nucleic acid stain, stains living *E. coli* and *S. aureus* cells. PI (red channel) can enter bacterial cells through broken membranes to stain dead *E. coli* and *S. aureus* cells. In control images of bacteria alone without added Cu-MOFs, a bright green (live) signal with high contrast was observed in *E. coli* and *S. aureus* cells. When the bacteria cells were treated with 0.167 mg mL^{-1} Cu-MOFs, the emission in the red channel showed higher contrast in *E. coli* and *S. aureus* cells, suggesting that bacterial cells in the image had been effectively killed by Cu-MOFs. As mentioned above, this illustrates the excellent antibacterial properties of Cu-MOF due to an oxidative stress response, also revealing the antibacterial mechanism of Cu-MOFs that may be caused by the destruction of the cell membrane.

Cu^{2+} has a certain antibacterial effect. In order to verify that the antibacterial effect of the prepared Cu-MOFs came from its excellent oxidase activity rather than Cu^{2+} or AMTA, the structural stability of Cu-MOFs was explored before and after antibacterial treatment. The amount of Cu^{2+} in the supernatant before and after co-culture with bacteria was quantified by AAS and ICP-MS. The Cu^{2+} content in the supernatant before co-culture with bacteria determined according to the standard curve is 23.6 ng mL^{-1} (Fig. 7(A)). Compared with the supernatant before antibacterial treatment, there was no significant increase in Cu^{2+} (32.3 ng mL^{-1}) after co-culture with bacteria, indicating that the Cu-MOFs had good structural stability, and framework collapse would not occur. By changing Cu^{2+} concentration, a dose-dependent study of antibacterial performance against *E. coli* and *S. aureus* of Cu^{2+} (20 and 100 ng mL^{-1} prepared from $Cu(NO_3)_2$) was conducted. As shown in Fig. 7 (B), compared with the control group without adding Cu^{2+}, the survival rate of the bacteria (*E. coli* and *S. aureus*) did not decrease when the Cu^{2+} concentration was 20 ng mL^{-1}, and even at a very high concentration (100 ng mL^{-1}) it showed neg-

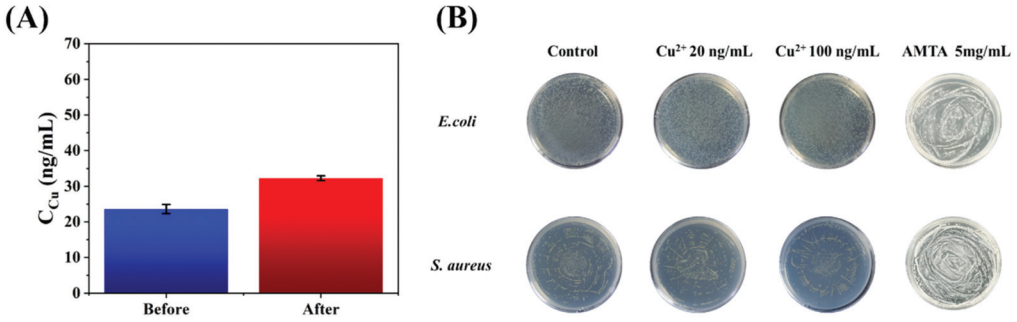

Fig. 7 (A) The Cu^{2+} content in the supernatant before and after co-incubation with bacteria. (B) Antibacterial performance against *E. coli* and *S. aureus* in the corresponding different concentrations of Cu^{2+} and AMTA.

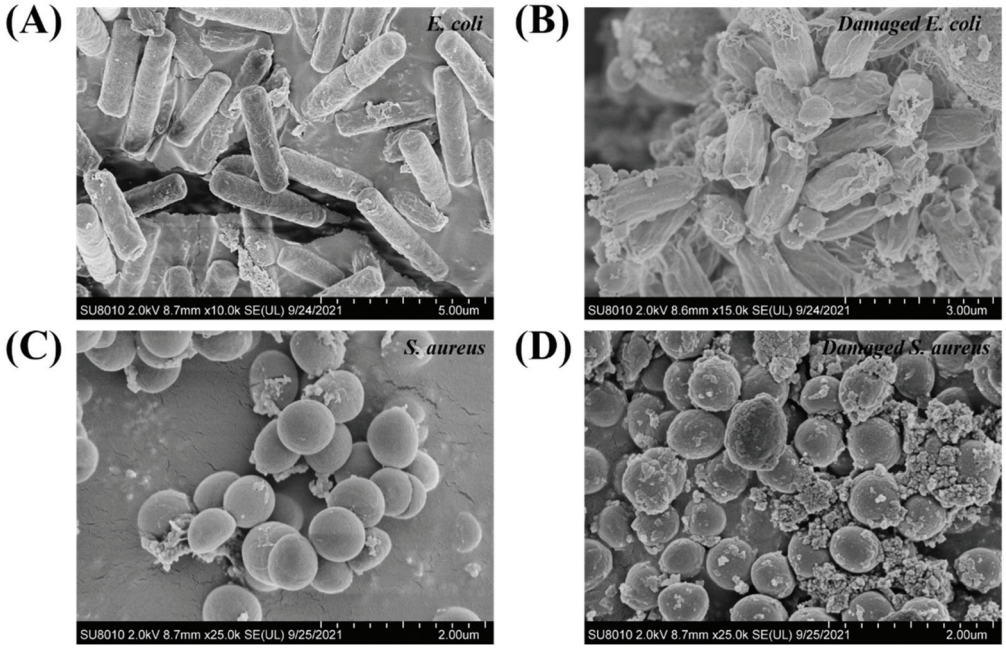

Fig. 8 SEM morphological images of bacteria: normal and damaged *E. coli* (A and B); normal and damaged *S. aureus* (C and D).

ligible antibacterial activity, and for AMTA alone (5 mg mL^{-1}), no obvious antibacterial activity was found. That shows that high-efficiency oxidase activity is the main reason for the excellent antibacterial effect of Cu-MOFs.

In order to understand the morphological effects on different kinds of bacteria in the presence of Cu-MOFs, the morphological changes in *E. coli* and *S. aureus* cells were observed by SEM. Fig. 8(A) shows that normal *E. coli* have a complete and smooth outer membrane. After co-incubation with Cu-MOFs (Fig. 8(B)), the ROS produced by Cu-MOFs caused serious oxidative damage to the outer membrane, and the outer membrane was seriously damaged with obvious folds. Fig. 8(C) and (D) indicated that *S. aureus* could hardly maintain their normal cell morphology after co-incubation with Cu-MOFs. The cytoplasm of bacteria flew out after the membrane was damaged, resulting in the death of the bacteria. Above all this showed that Cu-MOFs have a strong inhibitory effect on *E. coli* and *S. aureus*, and the oxidative damage to the bacterial membrane leads to the death of the bacteria.

4 Conclusion

In this work, a novel strategy was adopted to construct an oxidase-like nanozyme (Cu-MOFs) according to the blueprint of a natural enzyme. The well-defined tailorable cavities of Cu-MOFs can offer a hydrophobic coordination environment similar to that of natural enzymes. Compared with natural enzymes, Cu-MOFs with a reactive copper core have a stronger oxygen activation ability without the addition of H_2O_2 and higher stability. Antibacterial test results indicated that Cu-MOFs displayed good broad-spectrum antibacterial ability at low concentration, strong oxidase activity leading to wrinkle changes and functional inactivation of bacterial cell mem-

branes. Our work reveals that oxidase Cu-MOFs show potential in catalysis and bacterial control.

Conflicts of interest

The authors declare that they have no known competing financial interests or personal relationships that could have appeared to influence the work reported in this paper.

Acknowledgements

This work was supported by the National Natural Science Foundation of China (Grant No. 61875114 and 62005156).

References

1 H. Wei and E. Wang, *Chem. Soc. Rev.*, 2013, **42**, 6060–6093.
2 J. Kim, J. W. Grate and W. Ping, *Trends Biotechnol.*, 2008, **26**, 639–646.
3 H. Wei, C. G. Chen, B. Y. Han and E. K. Wang, *Anal. Chem.*, 2008, **80**, 7051–7055.
4 P. Anjani, A. Nagvenkar and A. Gedanken, *ACS Appl. Mater. Interfaces*, 2016, **8**, 22301–22308.
5 W. He, X. Wu, J. Liu, X. Hu, K. Zhang, S. Hou, W. Zhou and S. Xie, *Chem. Mater.*, 2010, **22**, 2988–2994.
6 L. Mi, Y. Sun, L. Shi and T. Li, *ACS Appl. Mater. Interfaces*, 2020, **12**, 7879–7887.
7 Y. M. Park, Y. S. Choi, H. R. Lee, S. H. Yun and S. J. Lee, *Biosens. Bioelectron.*, 2020, **161**, 112252.
8 A. R. Vazquez-Duhalt, *Chem. Biol.*, 2002, **9**, 555–565.
9 R. A. Lawrence and R. F. Burk, *Biochem. Biophys. Res. Commun.*, 2012, **425**, 503–509.
10 Q. Wang, Z. Yang, X. Zhang, X. Xiao and B. Xu, *Angew. Chem., Int. Ed.*, 2010, **46**, 4285–4289.
11 T. K. Sau, A. L. Rogach, F. J. Ckel, T. A. Klar and J. Feldmann, *Adv. Mater.*, 2010, **22**, 1805–1825.
12 K. Li, N. J. Hogan, M. J. Kale, N. J. Halas and P. Christopher, *Nano Lett.*, 2017, **17**, 3710–3717.
13 K. Abdullah, G. Sevil, A. Osman, S. Atac and G. Kursad, *Neonatology*, 2005, **87**, 15–18.
14 X. Jiang, X. Wang, A. Lin and H. Wei, *Anal. Chem.*, 2021, **93**, 5954–5962.
15 Z. Peng, S. Dengrong, C. Ara, W. Seunghyun and L. Seonggyu, *Nat. Commun.*, 2019, **10**, 940.
16 A. A. Vernekar, T. Das, S. Ghosh and G. Mugesh, *Chem. – Asian J.*, 2016, **11**, 72–76.
17 M. Huo, L. Wang, Y. Chen and J. Shi, *Nat. Commun.*, 2017, **8**, 357.
18 Q. Liu, K. Wan, Y. Shang, Z. G. Wang and B. Ding, *Nat. Mater.*, 2021, **20**, 395–402.
19 S. Y. Lee, S. Y. Lim, D. Seo, J. Y. Lee and T. D. Chung, *Adv. Energy Mater.*, 2016, **6**, 1502207.
20 C. L. Coyle, W. G. Zumft, P. Kroneck, H. KÖRNER and W. Jakob, *FEBS J.*, 2010, **153**, 459–467.
21 R. J. Quinlan, M. D. Sweeney, L. L. Leggio and H. Otten, *Proc. Natl. Acad. Sci. U. S. A.*, 2011, **108**, 15079–15084.
22 Y. A. Bae, G. B. Cai, S. H. Kim, W. M. Sohn and Y. Kong, *Int. J. Parasitol.*, 2013, **43**, 891–900.
23 P. J. Klinman, *J. Biol. Chem.*, 2006, **281**, 3013–3016.
24 N. Fujieda, A. Hasegawa, K. I. Ishihama and S. Itoh, *Chem.–Asian J.*, 2012, **7**, 1203–1207.
25 N. A. Miti, S. J. Smith, A. Neves, L. W. Guddat, L. R. Gahan and G. Schenk, *Chem. Rev.*, 2006, **106**, 3338–3363.
26 J. W. Ginsbach, M. T. Kieber-Emmons, R. Nomoto and A. Noguchi, *Proc. Natl. Acad. Sci. U. S. A.*, 2012, **109**, 10793–10797.
27 K. P. Jensen and U. Ryde, *J. Biol. Chem.*, 2004, **279**, 14561–14569.
28 E. I. Solomon, *Inorg. Chem.*, 2016, **55**, 6364.
29 P. Wu, F. Fan, J. Song, W. Peng and B. Wang, *J. Am. Chem. Soc.*, 2019, **141**, 19776–19789.
30 X. Feng, Y. Song, J. S. Chen, Z. Xu and W. Lin, *J. Am. Chem. Soc.*, 2021, **143**, 1107–1118.
31 J. Vogt, R. Perozzo, A. Pautsch, A. Prota and G. E. Schulz, *Proteins: Struct., Funct., Bioinf.*, 2015, **41**, 545–553.
32 F. Fresno, R. Portela, S. Suárez and J. M. Coronado, *J. Mater. Chem. A*, 2014, **2**, 2863–2884.
33 R. R. Zhu, W. R. Wang, X. Y. Sun, H. Liu and S. L. Wang, *Toxicol. in Vitro*, 2010, **24**, 1639–1647.
34 H. L. Li, M. M. Eddaoudi, M. O'Keeffe and O. M. Yaghi, *Nature*, 1999, **402**, 272–279.
35 P. Li, S. Y. Moon, M. A. Guelta, L. Lin, D. Gómez-Gualdrón, R. Q. Snurr, S. P. Harvey, J. T. Hupp and O. K. Farha, *ACS Nano*, 2016, **10**, 9174–9182.
36 X. Lian, Y. Fang, E. Joseph, Q. Wang, J. Li, S. Banerjee, C. Lollar, X. Wang and H. C. Zhou, *Chem. Soc. Rev.*, 2017, **46**, 3386–3401.
37 C. Li, K. Wang, J. Li and Q. Zhang, *Nanoscale*, 2020, **12**, 7870–7874.
38 S. Horike, M. Dinca, K. Tamaki and J. R. Long, *J. Am. Chem. Soc.*, 2008, **130**, 5854–5855.
39 K. Wang, R. Bi, M. Huang, B. Lv, H. Wang, C. Li, H. Wu and Q. Zhang, *Inorg. Chem.*, 2020, **59**, 6808–6814.
40 Z. Yue, D. Haiyun, L. Yuan, F. Chunhuan and Y. Hu, *Chem. Commun.*, 2019, **55**, 3445–3448.
41 C. Li, K. Wang, J. Li and Q. Zhang, *ACS Mater. Lett.*, 2020, **2**, 779–797.
42 J. Liu, L. Y. Ye, W. H. Xiong, T. Liu, H. Yang and J. Lei, *Chem. Commun.*, 2021, **57**, 2820–2823.
43 J. Zhuang, Y. Duan, Q. Zhang, W. Gao and L. Zhang, *Nano Lett.*, 2020, **20**, 4051–4058.
44 L. Xinping, Y. Zhengqing, Z. Zhang, S. Yuhuan and R. Jinsong, *ACS Nano*, 2019, **13**, 5222–5230.
45 A. Association, *Am. Music Ther. Assoc.*, 2008, **272**, ED504518.
46 S. k. S. Bhattacharyya, R. Ali, M. Venkateswarulu and P. S. Mukherjee, *J. Am. Chem. Soc.*, 2020, **142**, 2020.
47 J. H. E. Cartwright, O. Piro and I. Tuval, *Phys. Rev. Lett.*, 2007, **98**, 165501.
48 E. S. Jeong, I. H. Hwang and S. W. Han, *Langmuir*, 2020, **36**, 10565–10576.

49 L. Pan, Q. Tao, S. Zhang, S. Wang, Z. Jian, S. Wang, Z. Wang and Z. Zhang, *Sol. Energy Mater. Sol. Cells*, 2012, **98**, 66–70.
50 L. Ottaviano, L. Lozzi, F. Ramondo, P. Picozzi and S. Santucci, *J. Electron Spectrosc. Relat. Phenom.*, 1999, **105**, 145–154.
51 C. Wyns, L. Derycke, B. Soenen, S. Bolca, D. Deforce, M. Bracke and A. Heyerick, *Talanta*, 2011, **85**, 197–205.
52 B. S. Razavi, B. Evgenia and K. Yakov, *Front. Microbiol.*, 2015, **6**, 1126.
53 T. Zhang, J. Liu, M. Fellner, C. Zhang, D. Sui and J. Hu, *Sci. Adv.*, 2017, **3**, e1700344.